

Aggregation-Induced Emission Artificial Enzyme (AIEzyme) with DNase-Like Activity: Imaging and Matrix Cleavage for Combating Bacterial Biofilm

Lei Han*, Yucui Zhang, Xuhui Bian, Baojian Huang

College of Chemistry and Pharmaceutical Sciences, Qingdao Agricultural University, 700 Changcheng Road, Qingdao 266109, Shandong, China.

* Corresponding author.

E-mail address: hanlei@qau.edu.cn

ABSTRACT: DNase-catalyzed hydrolysis of extracellular DNA (eDNA) have been widely employed to eradicate intractable biofilms. Although aggregation-induced emission (AIE) has become the ideal tool for killing planktonic bacteria, AIE luminogens (AIEgens) often lack DNase-mimetic activity, in order to suffer from poor anti-biofilm capacity. Here, an “AIEzyme”, a kind of AIE nanomaterial with enzyme-like activity, is designed and synthesized, where the AIEgens are used as the ligands of Zr-based coordination polymer nanoparticles. Not only do AIEzyme have enduring DNase-mimetic activity with high substrate affinity and low activation energy, but also structural rigidity-stabilized fluorescence. Due to the long-acting hydrolysis for eDNA in biofilm, AIEzyme can efficiently disorganize the established biofilms with good penetrability and realize the healing of superbugs-infected wound for at least seven days under only one dose of AIEzyme. Moreover, AIEzymes can be observed by virtue of their own AIE character, facilitating the study on self-positioning and residual amount of AIEzymes in wound. On the support of AIEzyme, we expect to explore an idea for the application development of AIEgen.

INTRODUCTION

DNA, the carrier of genetic information, is a highly stable polymer, which is linked by phosphate ester bond with the inert phosphate backbone.¹⁻³ The cleavage of the phosphate ester bond is essential for biological phenomena, biomedicine and biosensors.^{1, 4} For example, the DNase-catalyzed hydrolysis of phosphate ester bond by has been widely used for combating bacterial communities. Bacteria generally tend to attach to surfaces of organisms and settings by self-synthesized extracellular polymeric substances (EPS) to generate biofilm.⁵ In EPS, extracellular DNA (eDNA) plays the role of “bridge” and “glue” in connecting bacteria with other EPS components and enhancing bacterial adhesion, which is pivotal for the formation of mature and sessile bacterial communities.⁶⁻⁸ Under the aegis of EPS, biofilm-enclosed bacteria are prominently more resistant to antibiotics, reactive oxygen species (ROS), photothermal therapy, and host immune defenses than planktonic ones. So, biofilms involve in the majority of bacterial infections, causing chronic wounds, implant failure, persistent infections and even death.⁹⁻¹³ Although DNase and its composites have been recognized as anti-biofilm reagents to destroy eDNA and then eradicate intractable biofilms,¹⁴⁻¹⁶ they have some drawbacks including complicated preparation process, high cost and poor stability.¹⁷ Moreover, they generally fail to monitor their self-position during the antimicrobial process in real time, because of the lack of imaging function. Therefore, it is urgent to excavate a powerful agent to simultaneously realize the eDNA cleavage and imaging.

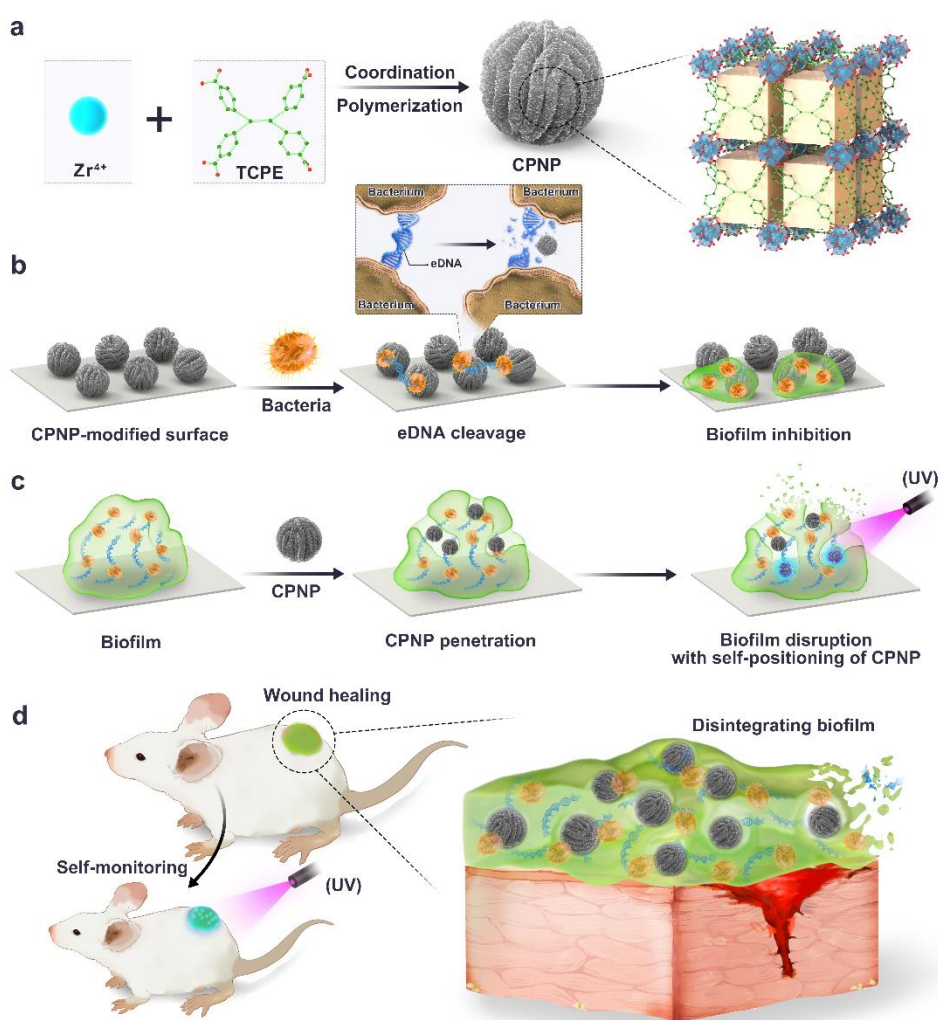
To expediently realize the real-time observation during the antimicrobial process, fluorescence imaging is highly desirable tool. However, the conventional fluorophores usually suffer from aggregation-caused quenching, greatly limiting their applications related to biology.¹⁸ As an opposite phenomenon, aggregation-induced emission (AIE) solved the above problem, where AIE luminogens (AIEgens) show no or weak fluorescence in dilute solution, but strong emissions in the aggregate or solid state, due to the restriction of intramolecular motion (RIM) mechanism.¹⁹⁻²⁴ So, AIEgens become a kind of ideal tools for

imaging microorganisms, cancer cells and so on.²⁵⁻²⁷ On the other hand, many AIEgens can also kill planktonic bacteria by photo-induced reactive oxygen species (ROS), photothermal effect and their own toxicity.²⁸⁻²⁹ However, they are expert at killing planktonic bacteria rather than anti-biofilm, because biofilm is markedly more resistant to environment stresses including ROS, high temperature and antibacterial agents. Therefore, it is interesting and meaningful to develop an AIEgen with imaging function and DNase-like activity for improving the biofilm resistance performance of AIE family.

Inspired by natural enzymes, nanozymes, an burgeoning type of nanomaterials with enzyme-like characteristics,³⁰⁻³¹ have attracted extensive interest due to their high catalytic activity, high stability and convenient preparation.³¹⁻³⁷ So far, the most of nanozymes show oxidoreductase-like character, and catalyze small molecular as substrates. In contrast, a few nanozymes mimic the activities of non-oxidoreductase, and catalyze macromolecule (such as DNA and protein) as substrate.^{4, 32} Although the cleavage of eDNA by DNase-like nanozymes has been reported less, DNase-like nanozymes still demonstrate the amazing application potential on biofilm disintegration.^{8, 38} Numerous studies have certified that the distinctive properties of nanozymes can stimulate their unique applications accordingly.^{36, 39-40} So, if DNase-mimicking nanozymes also possess AIE property, this will be very interesting and valuable scenario for disintegration and imaging of biofilm.

Here, we successfully synthesized Zr-based coordination polymer nanoparticle (CPNP) by using 1,1,2,2-tetra(4-carboxylphenyl)ethylene (TCPE, a typical AIEgen) as ligand. On the one hand, Zr-CPNPs showed stable fluorescence in various solvents and temperature due to the RIM effect in the rigid coordination structure. On the other hand, CPNPs showed outstanding DNase-mimetic activity with high substrate affinity and low activation energy, which can hydrolyze various DNAs including single-stranded DNA (ssDNA) and eDNA. So, we call the AIE nanomaterial with enzyme-like characteristics as “AIEzyme”. Due to the high-efficiency DNase-mimetic activity, good durability and strong penetrability,

AIEzyme not only enduringly prevented biofilm formation, but also dispersed mature biofilms. On account of the stable AIE character, AIEzyme also showed the capacity of imaging bacterial cell and self-positioning in biofilm. Particularly, CPNPs can maintain a prolonged and stable anti-biofilm efficiency on the superbugs-infected wound with acceptable safety, and simultaneously realize the real-time monitoring of AIEzyme residue (**Scheme 1**). We expect that the proposed AIEzyme would not only open an interesting avenue for the biofilm combating and the wound healing with process monitoring, but also provide a new opportunity for expanding the applications of AIEgens and nanozymes.



Scheme 1. Design of the CPNP AIEzyme for anti-biofilm applications. (a) Schematic preparation of CPNP. (b) Inhibition to bacterial adhesion and biofilm formation on CPNP-modified surface. (c) Dispersion of established biofilm after subsequent addition of CPNP and self-position of CPNP during the penetration into biofilm. (d) Wound healing by anti-biofilm capacity of CPNP and self-monitoring of CPNP in wound.

RESULTS AND DISCUSSION

2.1. Synthesis and Characterization of Zr-CPNPs. Zr-CPNPs were synthesized via the coordination polymerization approach at 90 °C with ZrCl₄ and AIE ligand (TCPE) as precursor (Scheme 1a) and emitted sky-blue fluorescence in solid state (**Figure 1a**). Scanning electron microscopy (SEM) and transmission electron microscopy (TEM) images demonstrate that CPNPs show well monodisperse and uniform walnut-like morphology with the average diameter of about 200 nm (Figure 1b). Chemical composition and distribution of CPNPs are confirmed by energy dispersive X-ray (EDX) spectroscopy (Figure 1c and Figure S1). Powder X-ray diffraction (PXRD) pattern of CPNPs (Figure 1d) gives well-resolved peaks, suggesting the high crystallinity. Fourier transform infrared spectrometry (FTIR) shows an obvious blueshift of -CO stretching frequency from 1682 cm⁻¹ to 1605 cm⁻¹ (Figure 1e), confirming the formation of CPNPs from Zr⁴⁺ ions and TCPE ligands.⁴¹

Dynamic light scattering (DLS) test shows that the hydration diameter of Zr-CPNPs was about 300 nm, suggesting the existence of hydration layer (Figure 1f). In addition, the hydrous size of CPNPs was stable within wide pH range (5–11), while the size increased sharply at pH 4 (Figure S2). To explain this phenomenon, the influence of pH on zeta potentials of CPNPs was investigated (Figure 1g). The surface charge of CPNPs tends to zero at pH 4, suggesting the isoelectric point is approximately at pH 4. So, the disappearance of electrostatic repulsion at pH 4 leads to the aggregation of CPNPs, but otherwise CPNPs have stable size due to the strong electrostatic repulsion when the pH is not near the isoelectric point.

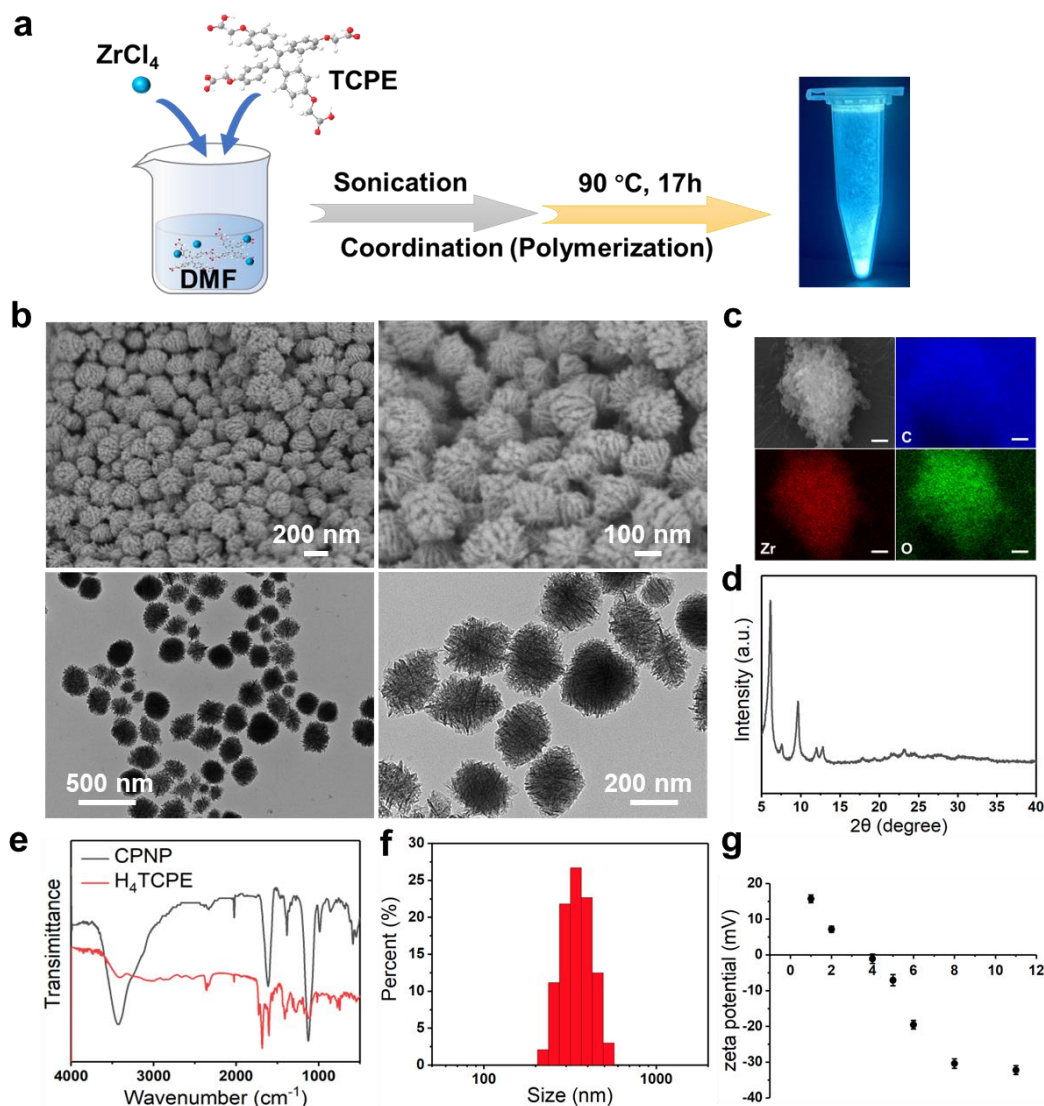


Figure 1. Synthesis and characterization of CPNPs. (a) Synthesis schematic of CPNPs and the fluorescent photo under 365 nm UV light. (b) SEM (top) and TEM (bottom) images of CPNPs at varied magnifications. (c) SEM and EDX elemental mapping images of CPNPs. Scale bars are 1 μm . (d) PXRD pattern. (e) FTIR spectra of CPNPs and TCPE. (f) DLS particle size distribution of CPNPs in aqueous solution (pH 8). (g) Zeta potentials of CPNP at different pH conditions.

2.2. Photophysical Properties of Zr-CPNPs. As expected, CPNPs emit bright sky-blue fluorescence under ultraviolet (UV) light in solution state (**Figure 2a**). Interestingly, the fluorescence of CPNPs shows negligible solvent effects (Figure 2b, 2c and S3). The excitation and emission spectra are not affected by the polarity of solvents, suggesting the negligible twisted intramolecular charge transfer effect in polar media. Considering temperature has a strong effect on the degree of rotation of these dynamic phenyl

rings, the fluorescence of CPNPs was researched at various temperatures (Figure 2d). Upon increasing temperature from 4 to 80 °C, the emission intensity of CPNPs at 470 nm gradually decreases. For many AIEgens, rotations of the phenyl rings speed up upon increasing temperature. So, the increased molecular motions can reduce and even quench the fluorescence.⁴² The temperature-dependent fluorescence of CPNPs is consistent with many other AIEgens.⁴²⁻⁴⁵ It's worth noting that the change in fluorescence intensity of CPNPs is much smaller than free ligand TCPE (Figure 2e and S4). These results strongly indicate that the phenyl ring rotors of CPNPs are partially restricted in the structure of CPNPs and then RIM effect in the rigid construction induces the stable emission. In addition, the fluorescence lifetime of CPNPs was determined to be 3.66 ns (Figure 2f). The absolute quantum yield of CPNPs is 18.6% in aqueous solution.

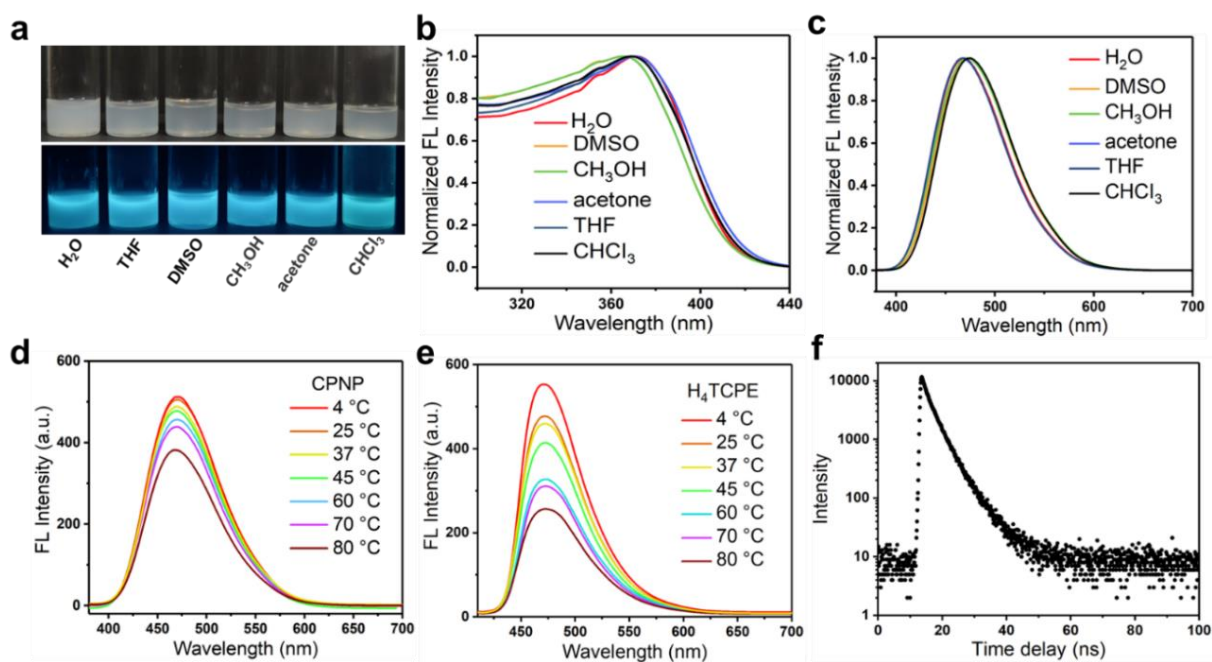


Figure 2. (a) Fluorescent photographs of CPNPs in solvents with different polarities under daylight and 365 nm UV irradiation. (b) Normalized excitation and (c) emission spectra of CPNPs in solvents with different polarities. Temperature-responsive emission of (d) CPNPs and (e) TCPE in aqueous solution ($\lambda_{\text{ex}} = 360$ nm). (f) Fluorescence decay curve of CPNPs in aqueous solution.

2.3. DNase-like activity of CPNPs. To comprehensively verify the DNase-like activity of CPNPs, various DNA model substrates including bis(4-nitrophenyl)phosphate (BNPP), ssDNA and bacterial genome DNA were employed (Figure 3a, 3e and 3g). As shown in Figure 3b and 3c, CPNPs can catalyze the hydrolysis of DNA dinucleotide analogue BNPP into nitrophenol, which has absorbance peak at 410 nm. To explore whether the DNase-like activity comes from the metal ion or the polymer monomer, the mixture of Zr^{4+} and TCPE were used to replace CPNPs and there was no observable absorption peak. These results indicate that DNase-mimetic activity occurs only after the formation of coordination polymer. In addition, the DNase-like activity of CPNPs shows pH-dependence and achieves highest activity at pH 8.0, (Figure 3d and S5), which is similar to natural DNase.⁴⁶

To further verify the DNase-like activity of CPNPs, the agarose gel (1%) electrophoresis was used on recording the hydrolysis of ssDNA under the catalysis of CPNPs (Figure 4f). Like DNase, CPNPs can effectively cleave ssDNA. Considering the bacterial genome DNA is similar to the eDNA in biofilms,⁴⁷⁻⁴⁸ the genomic DNA of *E. coli* and *S. aureus* was extracted and used as the substrate. As shown in the agarose gel electrophoresis (Figure 4h), the CPNPs can effectively degrade genomic DNA of MRSA into smaller fragments with increasing reaction time. Like DNase, CPNPs exhibit high catalytic activity for the hydrolysis of the genomic DNA from MRSA and *E. coli* and all the genomic DNA can be degraded within 2 h. In contrast, the control using the mixture of Zr^{4+} and TCPE shows that the genomic DNA remained stable under the same reaction conditions (Figure S6). These results confirm that the DNase-like activity indeed originate from the coordination of Zr^{4+} and TCPE, which is fit for various types of DNA. In addition, CPNPs did not show obvious degrading effect towards the other two main EPS components, polysaccharides and proteins (data not shown). Thus, CPNPs are expected to degrade eDNA when combating biofilms.

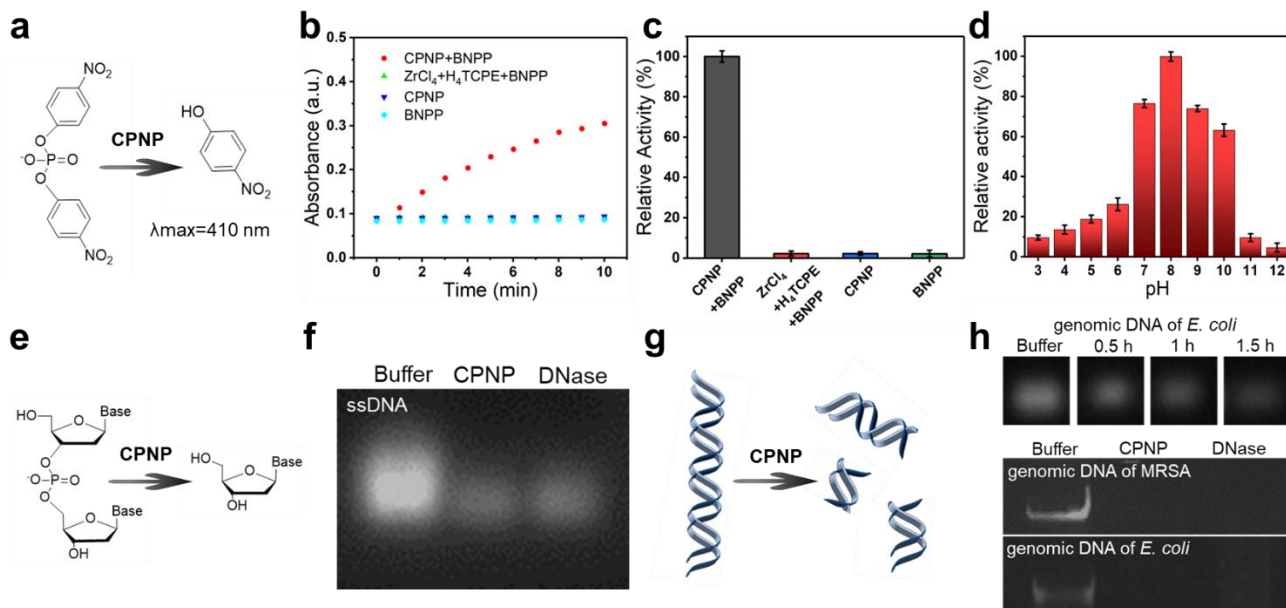


Figure 3. DNase-like activity of CPNPs. (a) Schematic diagram of BNPP hydrolyzation. (b) Time-dependent absorbance changes of nitrophenol at 410 nm in different systems (pH = 8.0). (c) The corresponding histogram of relative DNase-like activities. (d) The influence of pH on the DNase-like activity of CPNPs. (e) Schematic diagram of ssDNA hydrolyzation. (f) Agarose gel electrophoresis showing hydrolyzation of ssDNA under the catalysis of CPNPs and DNase for 0.5 h. (g) Schematic diagram of genomic DNA cleavage. (h) Cleavage of genomic DNA of *E. coli* by CPNPs for different incubation times, and cleavage of genomic DNA of MRSA and *E. coli* by CPNPs and DNase for 2 h incubation.

2.4. Catalytic Reaction Kinetics of CPNPs. To reasonably evaluate the DNase-mimetic activity of CPNPs, the steady-state kinetics was investigated by changing the concentration of BNPP at a fixed concentration of CPNPs. The initial reaction rate increases with the increase of BNPP (**Figure 4a**), further manifesting the DNase-mimetic activity of CPNPs. These data are conformed to the Michaelis-Menten equation (Figure 4b), and K_m of CPNPs for BNPP is 0.09 mM. In addition, the concentrations of BNPP (C_t) under the catalytic hydrolysis of CPNPs and DNase were monitored at various temperatures (Figure S7 and S8). The hydrolysis rate increases with the temperature, indicating the higher temperature would accelerate the interactions between reactants and catalysts. A good linear correlation of $\ln C_t$ (C_t indicate

the concentration of BNPP) versus reaction time (t) is observed (Figure. 4c), indicating the good pseudo-first-order kinetics of CPNPs, which is similar with DNase (Figure. 4d). So, the kinetic rate constant k are obtained to be $8.902 \times 10^{-2} \text{ min}^{-1}$ at 298 K, $1.270 \times 10^{-1} \text{ min}^{-1}$ at 308 K, $2.309 \times 10^{-1} \text{ min}^{-1}$ at 318 K, and $2.974 \times 10^{-1} \text{ min}^{-1}$ at 328 K, respectively, which are integrally higher than those of DNase ($2.968 \times 10^{-4} \text{ min}^{-1}$ at 298 K, $1.92 \times 10^{-3} \text{ min}^{-1}$ at 308 K, $1.779 \times 10^{-2} \text{ min}^{-1}$ at 318 K, and $5.742 \times 10^{-2} \text{ min}^{-1}$ at 328 K) (Figure 4e). According to Arrhenius equation, the activation energy (E_a) of the BNPP hydrolyzation catalyzed by CPNPs or DNase was calculated by plotting $\ln k$ versus $1/T$ (Figure. 4f and 4g). As shown in Figure 4h, the E_a value of CPNPs was 32.77 kJ/mol, which was dramatically smaller than the one of DNase (146.5 kJ/mol). The above results indicate that under the CPNPs, the minimum energy required for the occurrence of hydrolysis reaction is significantly reduced, which makes the reaction much easier.

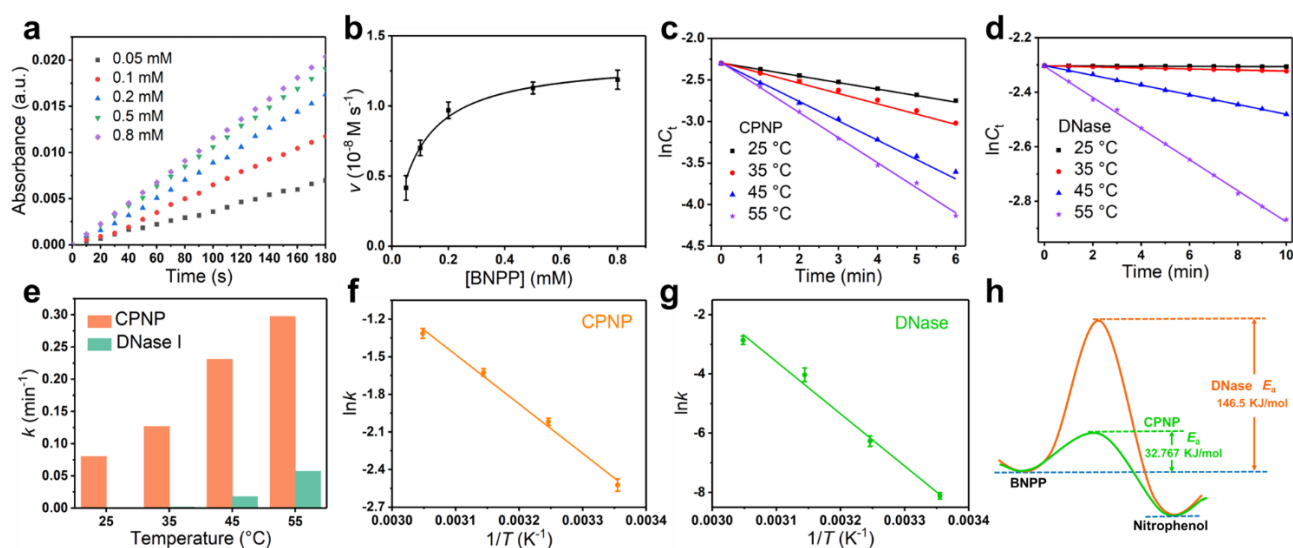


Figure 4. Kinetics assay for DNase-like activity of CPNPs. (a) Absorbance curves at 410 nm with time for CPNP-catalyzed hydrolyzation of BNPP in different concentrations (0–4 mM). (b) Michaelis–Menten curves fit for varied concentrations of BNPP. Plots of $\ln C_t$ versus reaction time (t) corresponding to the hydrolysis of BNPP under the catalysis of (c) CPNP and (d) DNase at various temperatures. (e) The comparison of k of CPNPs and DNase at various temperatures. Arrhenius plot of $\ln k$ versus $1/T$ in the temperature range of 298–328K for (f) CPNP and (g) DNase. (h) The activation barrier comparison under the catalysis of CPNPs and DNase.

2.5. Bacterial Imaging Based on AIEzyme. Considering CPNP simultaneously has the both of the AIE property and DNase-like activity, we call CPNP as “AIEzyme”, which represents a type of AIEgens with enzyme-like characteristics. On account of the AIE property of CPNPs, the bacteria staining performance of CPNPs on MRSA was evaluated. When incubating bacteria with CPNPs, the fluorescent signal can be clearly observed on bacterial cells with extremely low background fluorescence, showing the excellent bacterial imaging ability (Figure S9). To investigate the location of CPNPs on bacterial cells, CPNPs-strained cells were observed by SEM. CPNPs adsorb on the surfaces of cells, and all bacteria maintain their regular shape with well-defined cell walls and borders (Figure S10). The results verify not only the staining of AIEzyme on the surface of bacterial cell, but also the inherent hypotoxicity of AIEzyme to bacteria.

2.6. Prohibiting Biofilm Generation by AIEzyme. These above results inspired us to evaluate the anti-biofilm performance of AIEzyme. So, its ability of prohibiting bacterial adhesion and biofilm generation was investigated (Scheme 1b). MRSA suspensions were statically incubated with CPNP- and DNase I-coated glass slides for different lengths of time. As for crystal violet staining assay (Figure 5a), MRSA are abundantly adhered to the bare surfaces, while the adhesions of bacteria to CPNP- and DNase-coated surfaces are obviously reduced. Interestingly, biomass attached on the DNase-coated surface significantly increases after 24 h, while dramatically reduced adhesion biofilm is observed on the CPNP-coated surfaces even after 120 h (Figure 5b). Then, 3D confocal laser scanning microscopy (CLSM) demonstrates that the biofilm formation is intensively inhibited on CPNP-coated surfaces, obviously superior to DNase-coated surface (Figure 5c). With the aid of the excellent DNase-like activity of CPNPs, the average thickness of biofilms was less than 5 μm even after 24 h (Figure 5d), which was much thinner than the case on DNase-coated surfaces. To further confirm the anti-biofilm performance, *E. coli* were

employed, and the results is similar with MRSA (Figure S11).

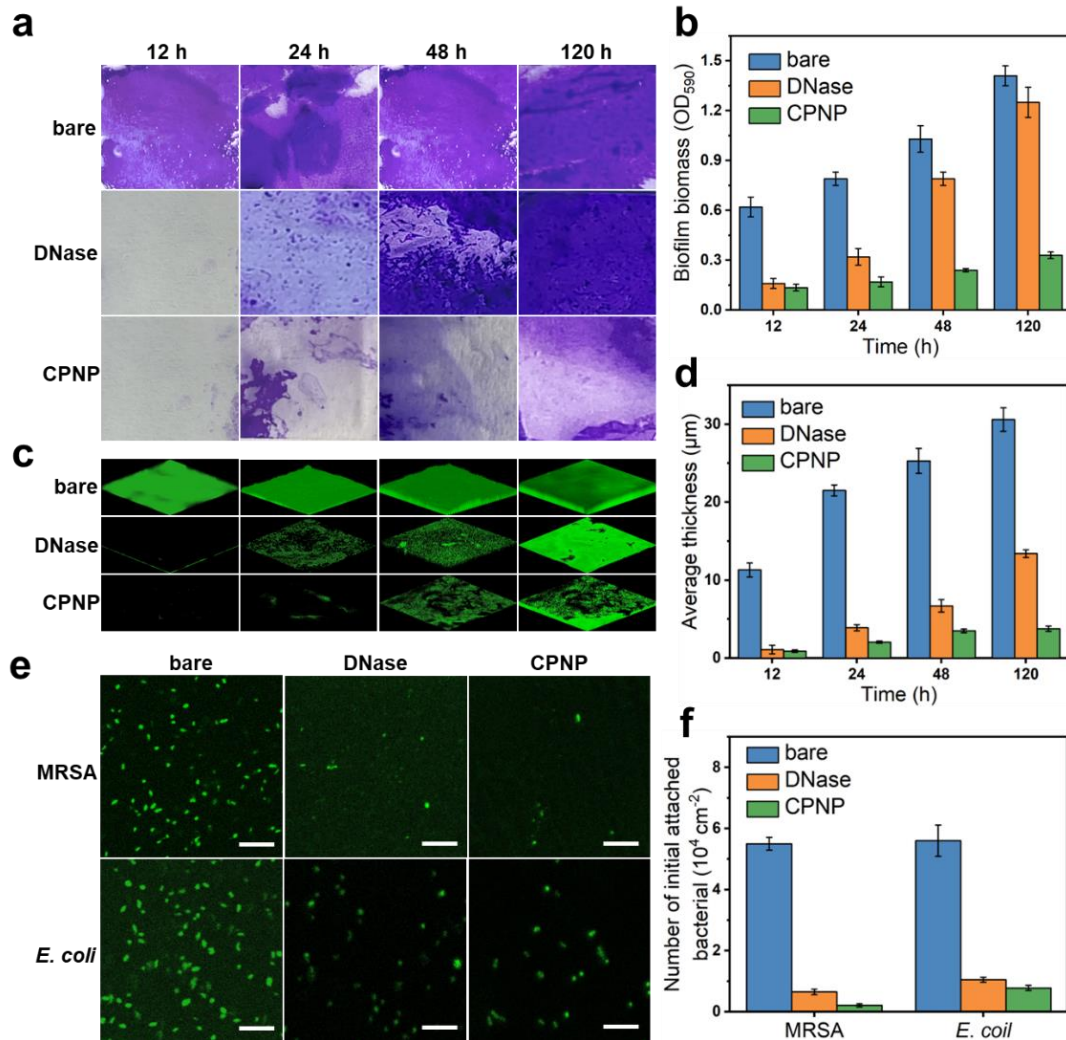


Figure 5. Inhibited biofilm formation on CPNP-modified surfaces. (a) Crystal violet-stained MRSA biofilms formed on bare, DNase-, and CPNPs-modified surfaces for different incubation times. (b) Quantitative biomass analysis of the crystal violet-stained MRSA biofilms. (c) 3D CLSM of the Calcein-AM-stained MRSA biofilms. Image sizes: 386.87 $\mu\text{m} \times 386.87 \mu\text{m}$. The bacteria were stained with Calcein-AM. (d) Average thickness of the MRSA biofilms. (e) CLSM images of initial attachment of MRSA and *E. coli* on bare, DNase- and CPNP-modified surfaces. Scale bar: 10 μm . The bacteria were stained with Calcein-AM. (f) The number of initial attached bacteria on different surfaces. Each bar represents the average of three independent experiments.

In addition, at the initial stage of the bacterial adhesion (after 60 min incubation), a lot of bacterial cells (MRSA and *E. coli*) are attached onto the bare surfaces (Figure 5e), while the adhesion amounts of bacteria

to the CPNPs- and DNase-coated surfaces are dramatically reduced by more than 86.07% and 81.25%, respectively, compared to the bare surface (Figure 5f). Although the both DNase and CPNP can reduce the bacteria adhesion amount, there is the obvious difference on the long-term anti-biofilm performance of DNase and CPNP, which could be attributed to the vulnerable structure of natural DNase and the good stability of CPNPs. Hence, AIEzyme has an excellent anti-biofilm performance superior to DNase.

2.7. Disorganizing Formed Biofilm by AIEzymes. To investigate whether AIEzyme can disperse formed biofilms (Scheme 1c), 24 h-old *E. coli* and MRSA biofilms were treated with different concentrations of CPNPs for 12 h (Figure 6a). The crystal violet staining and 3D CLSM demonstrate that the remaining biomass and average thickness of the biofilms are significantly diminished by CPNPs in a dose-dependent manner (Figure 6b). Further, the ability of CPNPs towards dispersing various ages of biofilms was evaluated (Figure 6c). DNase only causes the slight disruption for young biofilms (less than 12 h old), while CPNP strongly disintegrates biofilms at all time points (Figure 6d).

In general, the intact biofilms physically shield foreign materials from inward penetration in order to protect themselves. Considering the excellent anti-biofilm capacity of CPNPs, we speculated CPNPs could penetrate into the inside of biofilms (Scheme 1c). So, the location of CPNPs was observed by virtue of AIE property. CPNPs could effectively penetrate into the internal biofilms and even a few of CPNPs have arrived at the bottom of biofilm within 10 min (Figure 6e). This might be due to the synergetic effect of DNase-like activity and sedimentation of CPNPs. In addition, the low toxicity of CPNPs to bacteria (Figure 6f and Figure S10) excludes the possibility that the anti-biofilm ability of CPNPs is caused by the effect of CPNPs on cell viability. Taken together, it can be deduced that CPNPs can rapidly penetrate biofilms, deeply destroyed eDNA in order to interrupt the “bridge” all biofilm components and finally disorganize the biofilms. More interestingly, the deep penetration of CPNPs can be self-certified (Scheme

1c).

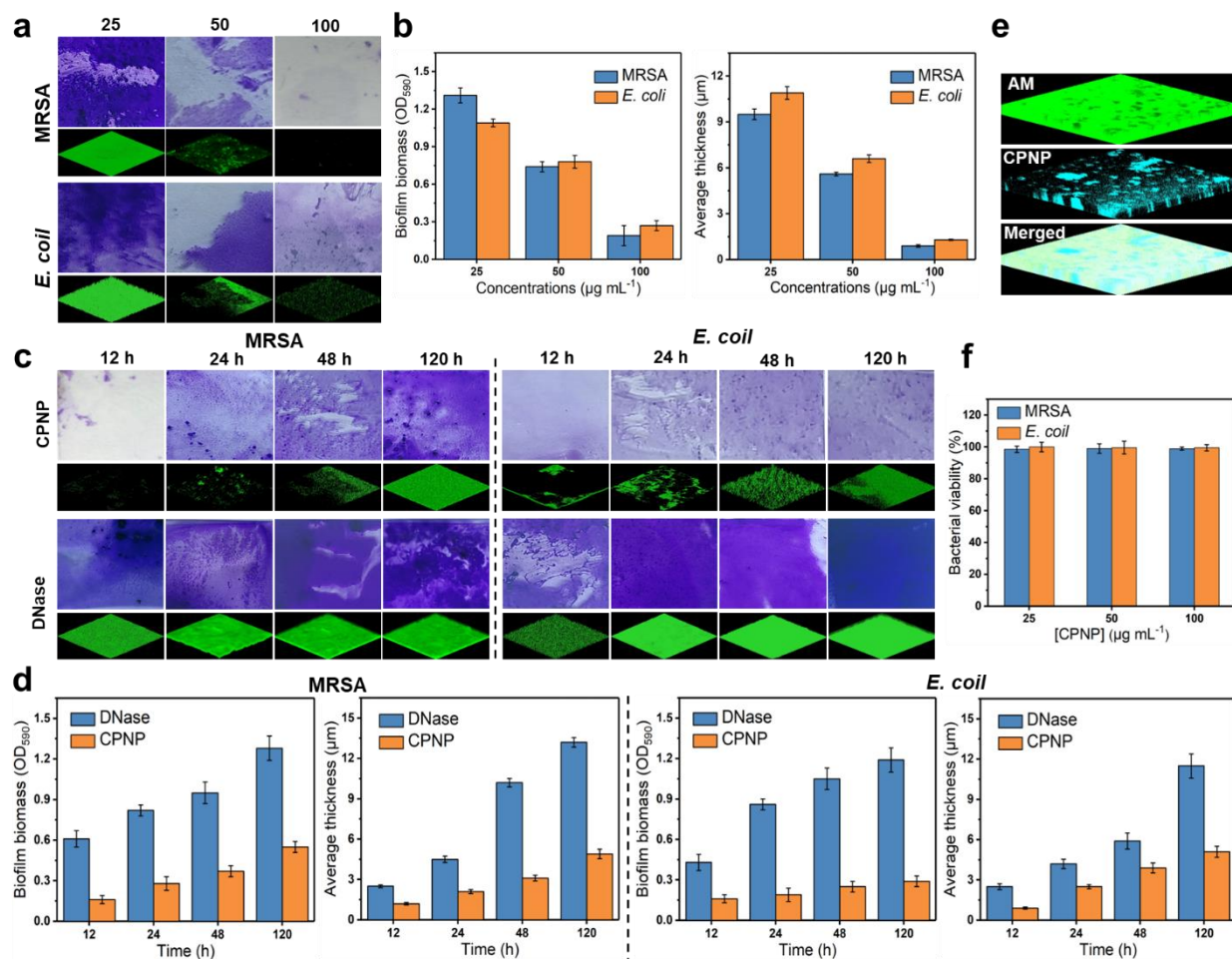


Figure 6. The disruption effect of CPNP on established biofilms. (a) Crystal violet staining and 3D CLSM images of 24 h-old MRSA and *E. coli* biofilms treated with different concentrations of CPNPs for 12 h. (b) Biomass and average thickness of the corresponding biofilms. (c) Crystal violet staining and 3D CLSM images of different ages of biofilms after treatment with CPNP (50 µg mL⁻¹). (d) Biomass and average thickness of the corresponding biofilms. (e) 3D CLSM imaging of MRSA biofilm after adding CPNPs (blue) on the biofilm for 10 min. The bacteria were stained with Calcein-AM (green). (f) Bacterial viability of MRSA and *E. coli* after incubation with different concentrations of CPNPs for 7 h. The size of each CLSM image was 386.87 µm × 386.87 µm. All each bar represents the average of three independent experiments.

2.8. In vivo antibacterial therapy and wound healing. To assess the *in vivo* anti-biofilm and wound healing performance of AIEzyme, a circular full-thickness skin wound model (0.5 cm diameter) on the

backs of mice was infected with MRSA (**Figure 7a**). The mice were separated into two groups treated with phosphate buffer saline (PBS), and CPNPs, respectively. To monitor visually the therapeutic effects, the wound healing processes were photographed over time, and the infected mice in CPNPs group achieved almost full recovery on 7th day (Figure 7b and 7c). In the contrast, the infected mice without CPNPs exhibit delayed recovery and partial recovery is observed on 7th day. It's worth noting that only one dose of CPNPs was administered on the first day (Figure 7a). To investigate the reason of the long-acting wound healing performance, the healing process of a larger wound (1 cm diameter) was recorded to visually monitor the durability of CPNPs by AIE property of CPNPs. As shown in Figure 7d, the fluorescence of CPNPs persists at the wound even on the 7th day. Further, SEM result indicated the morphology and structure of CPNPs were stable in physiological saline (Figure. S12). Moreover, the DNase-like activity of CPNPs remained stable and reusable over at least five catalytic cycles (Figure S13).

Taken together, the efficient, durable and irradiation-free wound healing capacity of CPNP AIEzymes could stem from persistent existence of AIEzymes on wound and long-acting DNase-like activity of AIEzymes. In contrast, many common AIEgens kill bacteria by photo-generated ROS, photothermal effect and their own toxicity.^{26, 49-51} So, for general antibacterial methods based on AIEgens, the regular irradiation and dressing change are usually required.⁵²⁻⁵⁴ As for the proposed anti-biofilm method based on AIEzymes (Figure 7a), the irradiation and the dressing change are not required, avoiding the frequent operations and the exogenous infection. Because the DNase-like activity of AIEzymes can continuously catalyze the hydrolyzation of eDNA in EPS without irradiation, AIEzymes can eliminate recurrence of biofilms and realize persistent anti-infection. More interestingly, the AIEzymes added on the wound can be monitored in real time by their own AIE property. Therefore, AIEzymes would show great application potential for anti-biofilm and wound healing.

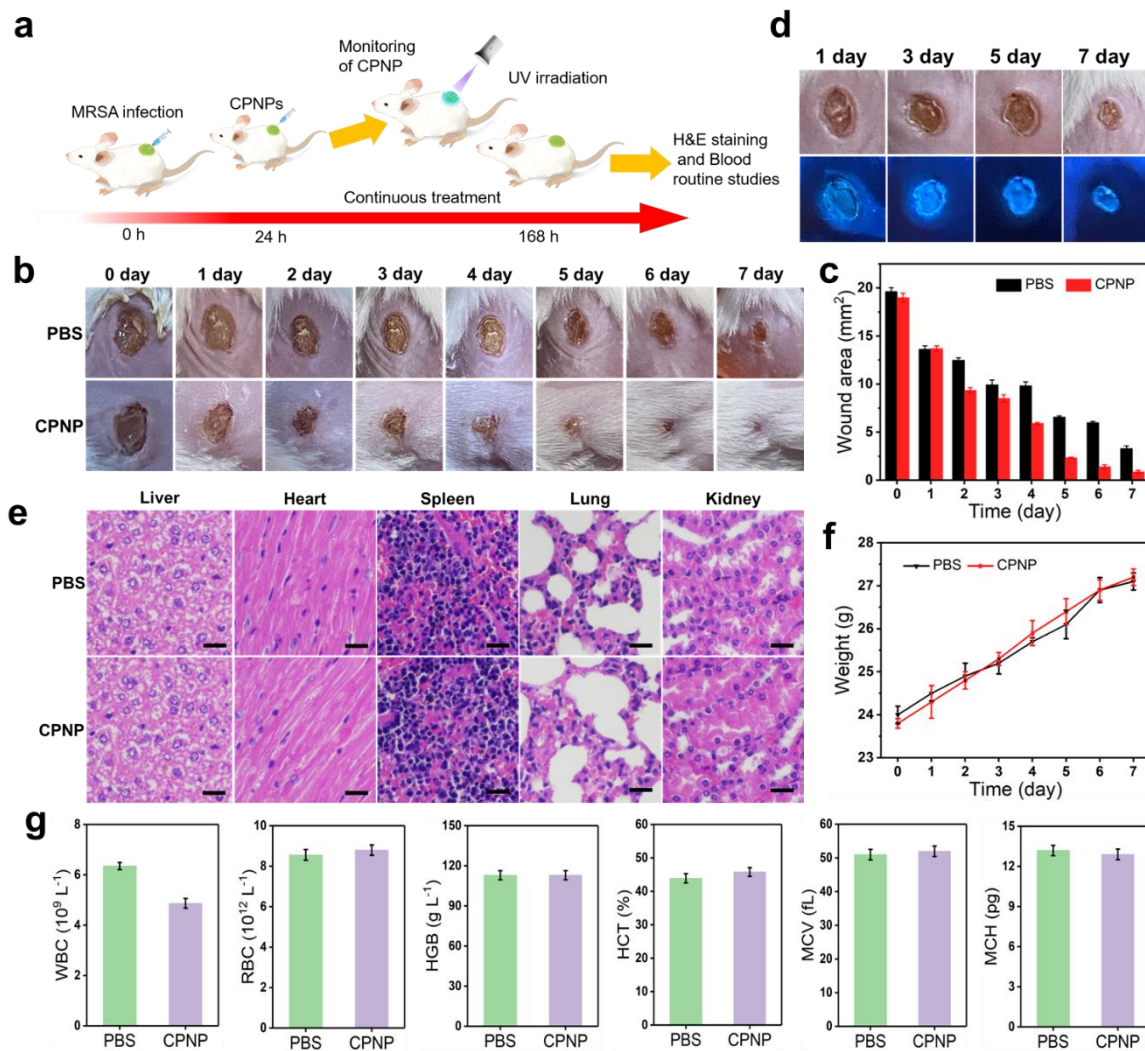


Figure 7. In vivo wound healing based on CPNP. (a) Schematic diagram of experimental design of mouse wound. (b) Photographs of the MRSA-infected wounds of mice during treatment with control (PBS) and CPNP. (c) Size changes of the infected wound of mice. (d) Photographs of CPNP residues in infected wound under a UV lamp (365 nm). (e) H&E staining of the liver, heart, spleen, lung and kidney sections from mice after 7 days treatment. Scale bar is 20 μm. (f) Body weights of the mice during 7 days of treatment. (g) Blood routine analysis of the mice treated with PBS or CPNP after 7 days treatment.

To investigate the biosafety of CPNPs, the hematoxylin and eosin (H&E) staining of organs (liver, heart, spleen, lung and kidney) was performed, which showed no observable organ damage and inflammatory lesion for CPNPs treatment (Figure 7e). Further, the bodyweight of the infected mice was monitored (Figure 7f), which showed a similar trend regardless of the treatment. Moreover, blood routine results

suggest that there is no difference between these mice with and without CPNPs treatment (Figure 7g). The above results demonstrate that CPNP AIEzyme has reliable biocompatibility and negligible biotoxicity.

CONCLUSIONS

In summary, we demonstrated the rational design of an “AIEzyme”, a kind of AIE nanomaterial with enzyme-like characteristics for biofilm combating with process monitoring. Due to the high substrate affinity, low activation energy and stable structure, AIEzyme shows high and enduring DNase-mimetic activity to hydrolyze eDNA in EPS of biofilm, which can prevent biofilm formation and disorganize established biofilms with good penetrability for prolonged period. Due to the AIE character and RIM effect in the rigid structure, AIEzyme shows stable fluorescence for bacterial cell imaging and self-positioning in biofilm. Combining with above merits, CPNPs can maintain a long-acting anti-biofilm capacity on the superbugs-infected wound with acceptable safety, and simultaneously realize the real-time monitoring of AIEzyme residue. The as-prepared AIEzyme with DNase-mimetic activity would not only provide an effective anti-biofilm tool for the wound healing with process monitoring, but also open a viable avenue for the application development of AIEgens and nanozymes.

ASSOCIATED CONTENT

Supporting Information

Detailed experimental procedures and supplemental figures (PDF)

AUTHOR INFORMATION

Corresponding Authors

Lei Han – *College of Chemistry and Pharmaceutical Sciences, Qingdao Agricultural University, 700 Changcheng Road, Qingdao 266109, Shandong, China.*

Authors

Yucui Zhang – *College of Chemistry and Pharmaceutical Sciences, Qingdao Agricultural University, 700 Changcheng Road, Qingdao 266109, Shandong, China.*

Xuhui Bian – *College of Chemistry and Pharmaceutical Sciences, Qingdao Agricultural University, 700 Changcheng Road, Qingdao 266109, Shandong, China.*

Baojian Huang – *College of Chemistry and Pharmaceutical Sciences, Qingdao Agricultural University, 700 Changcheng Road, Qingdao 266109, Shandong, China.*

Author contributions

L.H. conceived and supervised the work. Y.Z., X.B. and B.H. performed the experiments, and L.H. analyzed the results. L.H. wrote and revised the manuscript with input from all the other coauthors.

Notes

The authors declare no competing financial interest.

ACKNOWLEDGMENTS

This work was financially supported by National Natural Science Foundation of China (Grant No. 21705087), Youth Innovation Team Project for Talent Introduction and Cultivation in Universities of Shandong Province, Research Foundation for Distinguished Scholars of Qingdao Agricultural University (663-1117015).

REFERENCES

1. Yang, H.; Gao, P.; Rajashankar, K. R.; Patel, D. J., PAM-Dependent Target DNA Recognition and Cleavage by C2c1 CRISPR-Cas Endonuclease. *Cell* **2016**, *167*, 1814–1828.
2. Li, Q.; Tong, Z.; Cao, Y.; Gu, H., DNAs Catalyzing DNA Nanoconstruction. *Chem* **2021**, *7*, 2556–2568.
3. Hussmann, J. A.; Ling, J.; Ravisankar, P.; Yan, J.; Cirincione, A.; Xu, A.; Simpson, D.; Yang, D.; Bothmer, A.; Cotta-Ramusino, C.; Weissman, J. S.; Adamson, B., Mapping The Genetic Landscape of DNA Double-Strand Break Repair. *Cell* **2021**, *184*, 5653–5669.
4. Fang, R.; Liu, J., Cleaving DNA by Nanozymes. *J. Mater. Chem. B* **2020**, *8*, 7135–7142.
5. Thiyagarajan, D.; Das, G.; Ramesh, A., Extracellular-DNA-Targeting Nanomaterial for Effective Elimination of Biofilm. *ChemNanoMat* **2016**, *2*, 879–887.
6. Buzzo, J. R.; Devaraj, A.; Gloag, E. S.; Jurcisek, J. A.; Robledo-Avila, F.; Kesler, T.; Wilbanks, K.; Mashburn-Warren, L.;

- Balu, S.; Wickham, J.; Novotny, L. A.; Stoodley, P.; Bakaletz, L. O.; Goodman, S. D., Z-Form Extracellular DNA is a Structural Component of The Bacterial Biofilm Matrix. *Cell* **2021**, *184*, 5740–5758.
7. Yang, Y.; Li, M.; Zheng, X.; Ma, H.; Nerenberg, R.; Chai, H., Extracellular DNA Plays A Key Role in The Structural Stability of Sulfide-Based Denitrifying Biofilms. *Sci. Total Environ.* **2022**, *838*, 155822.
 8. Chen, Z.; Ji, H.; Liu, C.; Bing, W.; Wang, Z.; Qu, X., A Multinuclear Metal Complex Based DNase-Mimetic Artificial Enzyme: Matrix Cleavage for Combating Bacterial Biofilms. *Angew. Chem., Int. Ed.* **2016**, *55*, 10732–10736.
 9. Ciofu, O.; Moser, C.; Jensen, P. Ø.; Høiby, N., Tolerance and Resistance of Microbial Biofilms. *Nat. Rev. Microbiol.* **2022**.
 10. Rumbaugh, K. P.; Sauer, K., Biofilm Dispersion. *Nat. Rev. Microbiol.* **2020**, *18*, 571–586.
 11. Davies, D., Understanding Biofilm Resistance to Antibacterial Agents. *Nat. Rev. Drug Discovery* **2003**, *2*, 114–122.
 12. Epstein, A. K.; Pokroy, B.; Seminara, A.; Aizenberg, J., Bacterial Biofilm Shows Persistent Resistance to Liquid Wetting and Gas Penetration. *Proc. Natl. Acad. Sci.* **2011**, *108*, 995–1000.
 13. Anderson, G. G.; Palermo, J. J.; Schilling, J. D.; Roth, R.; Heuser, J.; Hultgren, S. J., Intracellular Bacterial Biofilm-Like Pods in Urinary Tract Infections. *Science* **2003**, *301*, 105–107.
 14. Swartjes, J.; Das, T.; Sharifi, S.; Subbiahdoss, G.; Sharma, P. K.; Krom, B. P.; Busscher, H. J.; van der Mei, H. C., A Functional DNase I Coating to Prevent Adhesion of Bacteria and the Formation of Biofilm. *Adv. Funct. Mater.* **2013**, *23*, 2843–2849.
 15. Tan, Y.; Ma, S.; Leonhard, M.; Moser, D.; Ludwig, R.; Schneider-Stickler, B., Co-Immobilization of Cellobiose Dehydrogenase and Deoxyribonuclease I on Chitosan Nanoparticles against Fungal/Bacterial Polymicrobial Biofilms Targeting both Biofilm Matrix and Microorganisms. *Mater. Sci. Eng. C* **2020**, *108*, 110499.
 16. Baelo, A.; Levato, R.; Julián, E.; Crespo, A.; Astola, J.; Gavalda, J.; Engel, E.; Mateos-Timoneda, M. A.; Torrents, E., Disassembling Bacterial Extracellular Matrix with DNase-Coated Nanoparticles to Enhance Antibiotic Delivery in Biofilm Infections. *J. Controlled Release* **2015**, *209*, 150–158.
 17. Liu, Z.; Wang, F.; Ren, J.; Qu, X., A Series of MOF/Ce-Based Nanozymes with Dual Enzyme-Like Activity Disrupting Biofilms and Hindering Recolonization of Bacteria. *Biomaterials* **2019**, *208*, 21–31.
 18. Wang, D.; Tang, B. Z., Aggregation-Induced Emission Luminogens for Activity-Based Sensing. *Acc. Chem. Res.* **2019**, *52*, 2559–2570.
 19. Luo, J.; Xie, Z.; Lam, J. W. Y.; Cheng, L.; Chen, H.; Qiu, C.; Kwok, H. S.; Zhan, X.; Liu, Y.; Zhu, D.; Tang, B. Z., Aggregation-Induced Emission of 1-methyl-1,2,3,4,5-pentaphenylsilole. *Chem. Commun.* **2001**, 1740–1741.
 20. Zhao, Z.; Zhang, H.; Lam, J. W. Y.; Tang, B. Z., Aggregation-Induced Emission: New Vistas at the Aggregate Level. *Angew. Chem., Int. Ed.* **2020**, *59*, 9888–9907.
 21. Kang, M.; Zhang, Z.; Song, N.; Li, M.; Sun, P.; Chen, X.; Wang, D.; Tang, B. Z., Aggregation-Enhanced Theranostics: AIE Sparkles in Biomedical Field. *Aggregate* **2020**, *1*, 80–106.
 22. Li, Z.; Ji, X.; Xie, H.; Tang, B. Z., Aggregation-Induced Emission-Active Gels: Fabrications, Functions, and Applications. *Adv. Mater.* **2021**, *33*, 2100021.
 23. Yan, D.; Wu, Q.; Wang, D.; Tang, B. Z., Innovative Synthetic Procedures for Luminogens Showing Aggregation-Induced Emission. *Angew. Chem., Int. Ed.* **2021**, *60*, 15724–15742.
 24. Mei, J.; Hong, Y.; Lam, J. W. Y.; Qin, A.; Tang, Y.; Tang, B. Z., Aggregation-Induced Emission: The Whole Is More Brilliant than the Parts. *Adv. Mater.* **2014**, *26*, 5429–5479.
 25. Li, H.; Kim, H.; Han, J.; Nguyen, V.-N.; Peng, X.; Yoon, J., Activity-Based Smart AIEgens for Detection, Bioimaging, and Therapeutics: Recent Progress and Outlook. *Aggregate* **2021**, *2*, e51.
 26. Borjihan, Q.; Wu, H.; Dong, A.; Gao, H.; Yang, Y.-W., AIEgens for Bacterial Imaging and Ablation. *Adv. Healthcare Mater.* **2021**, *10*, 2100877.
 27. He, X.; Lam, J. W. Y.; Kwok, R. T. K.; Tang, B. Z., Real-Time Visualization and Monitoring of Physiological Dynamics by Aggregation-Induced Emission Luminogens (AIEgens). *Annu. Rev. Anal. Chem.* **2021**, *14*, 413–435.
 28. Bai, H.; He, W.; Chau, J. H. C.; Zheng, Z.; Kwok, R. T. K.; Lam, J. W. Y.; Tang, B. Z., AIEgens for Microbial Detection and Antimicrobial Therapy. *Biomaterials* **2021**, *268*, 120598.

29. Zhang, H.; Jiang, W.; Peng, Y.; Yang, J.; Chu, X.; Long, Z.; Li, R.; Liang, Q.; Suo, H.; Wang, S.; Yang, M.; Qi, J.; Ding, D.; Yang, Y.-W.; Wang, B., Killing Three Birds with One Stone: Near-Infrared Light Triggered Nitric Oxide Release for Enhanced Photodynamic and Anti-Inflammatory Therapy in Refractory Keratitis. *Biomaterials* **2022**, *286*, 121577.
30. Gao, L.; Zhuang, J.; Nie, L.; Zhang, J.; Zhang, Y.; Gu, N.; Wang, T.; Feng, J.; Yang, D.; Perrett, S.; Yan, X., Intrinsic Peroxidase-Like Activity of Ferromagnetic Nanoparticles. *Nat. Nanotechnol.* **2007**, *2*, 577–583.
31. Wei, H.; Wang, E., Nanomaterials with Enzyme-Like Characteristics (Nanozymes): Next-Generation Artificial Enzymes. *Chem. Soc. Rev.* **2013**, *42*, 6060–6093.
32. Wu, J.; Wang, X.; Wang, Q.; Lou, Z.; Li, S.; Zhu, Y.; Qin, L.; Wei, H., Nanomaterials with Enzyme-Like Characteristics (Nanozymes): Next-Generation Artificial Enzymes (II). *Chem. Soc. Rev.* **2019**, *48*, 1004–1076.
33. Huang, Y.; Ren, J.; Qu, X., Nanozymes: Classification, Catalytic Mechanisms, Activity Regulation, and Applications. *Chem. Rev.* **2019**, *119*, 4357–4412.
34. Zhang, J.; Liu, J., Nanozyme-Based Luminescence Detection. *Luminescence* **2020**, *35*, 1185–1194.
35. Ai, Y.; Hu, Z.-N.; Liang, X.; Sun, H.-b.; Xin, H.; Liang, Q., Recent Advances in Nanozymes: From Matters to Bioapplications. *Adv. Funct. Mater.* **2022**, *32*, 2110432.
36. Jiao, L.; Yan, H.; Wu, Y.; Gu, W.; Zhu, C.; Du, D.; Lin, Y., When Nanozymes Meet Single-Atom Catalysis. *Angew. Chem. Int. Ed.* **2020**, *59*, 2565–2576.
37. Liang, M.; Yan, X., Nanozymes: From New Concepts, Mechanisms, and Standards to Applications. *Acc. Chem. Res.* **2019**, *52*, 2190–2200.
38. Hu, H.; Kang, X.; Shan, Z.; Yang, X.; Bing, W.; Wu, L.; Ge, H.; Ji, H., A DNase-Mimetic Artificial Enzyme for The Eradication of Drug-Resistant Bacterial Biofilm Infections. *Nanoscale* **2022**, *14*, 2676–2685.
39. Wu, J.; Li, S.; Wei, H., Multifunctional Nanozymes: Enzyme-Like Catalytic Activity Combined with Magnetism and Surface Plasmon Resonance. *Nanoscale Horiz.* **2018**, *3*, 367–382.
40. Wang, D.; Wu, H.; Phua, S. Z. F.; Yang, G.; Qi Lim, W.; Gu, L.; Qian, C.; Wang, H.; Guo, Z.; Chen, H.; Zhao, Y., Self-Assembled Single-Atom Nanozyme for Enhanced Photodynamic Therapy Treatment of Tumor. *Nat. Commun.* **2020**, *11*, 357.
41. Jung, S.; Oh, M., Monitoring Shape Transformation from Nanowires to Nanocubes and Size-Controlled Formation of Coordination Polymer Particles. *Angew. Chem., Int. Ed.* **2008**, *47*, 2049–2051.
42. Zhang, Z.; Bilalis, P.; Zhang, H.; Gnanou, Y.; Hadjichristidis, N., Core Cross-Linked Multiarm Star Polymers with Aggregation-Induced Emission and Temperature Responsive Fluorescence Characteristics. *Macromol.* **2017**, *50*, 4217–4226.
43. Peng, Q.; Shuai, Z., Molecular Mechanism of Aggregation-Induced Emission. *Aggregate* **2021**, *2*, e91.
44. Chen, J.; Law, C. C. W.; Lam, J. W. Y.; Dong, Y.; Lo, S. M. F.; Williams, I. D.; Zhu, D.; Tang, B. Z., Synthesis, Light Emission, Nanoaggregation, and Restricted Intramolecular Rotation of 1,1-Substituted 2,3,4,5-Tetraphenylsiloles. *Chem. Mater.* **2003**, *15*, 1535–1546.
45. Dong, J.; Qiao, Z.; Pan, Y.; Peh, S. B.; Yuan, Y. D.; Wang, Y.; Zhai, L.; Yuan, H.; Cheng, Y.; Liang, H.; Liu, B.; Zhao, D., Encapsulation and Protection of Ultrathin Two-Dimensional Porous Organic Nanosheets within Biocompatible Metal–Organic Frameworks for Live-Cell Imaging. *Chem. Mater.* **2019**, *31*, 4897–4912.
46. Sakai, T.; Miyazaki, T.; Shin, D.-M.; Kim, Y.-S.; Qi, C.-F.; Fariss, R.; Munasinghe, J.; Wang, H.; Kovalchuk, A. L.; Kothari, P. H.; Fermaintt, C. S.; Atkinson, J. P.; Perrino, F. W.; Yan, N.; Morse, H. C., DNase-Active TREX1 Frame-Shift Mutants Induce Aerologic Autoimmunity in Mice. *J. Autoimmun.* **2017**, *81*, 13–23.
47. Lappann, M.; Claus, H.; Van Alen, T.; Harmsen, M.; Elias, J.; Molin, S.; Vogel, U., A Dual Role of Extracellular DNA During Biofilm Formation of *Neisseria Meningitidis*. *Mol. Microbiol.* **2010**, *75*, 1355–1371.
48. Li, W.; Wang, J. J.; Qian, H.; Tan, L.; Zhang, Z.; Liu, H.; Pan, Y.; Zhao, Y., Insights Into the Role of Extracellular DNA and Extracellular Proteins in Biofilm Formation of *Vibrio parahaemolyticus*. *Front. Microb.* **2020**, *11*, 813.
49. Zhou, T.; Hu, R.; Wang, L.; Qiu, Y.; Zhang, G.; Deng, Q.; Zhang, H.; Yin, P.; Situ, B.; Zhan, C.; Qin, A.; Tang, B. Z., An AIE-Active Conjugated Polymer with High ROS-Generation Ability and Biocompatibility for Efficient Photodynamic Therapy of Bacterial Infections. *Angew. Chem., Int. Ed.* **2020**, *59*, 9952–9956.
50. Lee, M. M. S.; Yan, D.; Chau, J. H. C.; Park, H.; Ma, C. C. H.; Kwok, R. T. K.; Lam, J. W. Y.; Wang, D.; Tang, B. Z.,

Highly efficient phototheranostics of macrophage-engulfed Gram-positive bacteria using a NIR luminogen with aggregation-induced emission characteristics. *Biomaterials* **2020**, *261*, 120340.

51. Mei, J.; Leung, N. L. C.; Kwok, R. T. K.; Lam, J. W. Y.; Tang, B. Z., Aggregation-Induced Emission: Together We Shine, United We Soar! *Chem. Rev.* **2015**, *115*, 11718–11940.

52. Li, Y.; Zhao, Z.; Zhang, J.; Kwok, R. T. K.; Xie, S.; Tang, R.; Jia, Y.; Yang, J.; Wang, L.; Lam, J. W. Y.; Zheng, W.; Jiang, X.; Tang, B. Z., A Bifunctional Aggregation-Induced Emission Luminogen for Monitoring and Killing of Multidrug-Resistant Bacteria. *Adv. Funct. Mater.* **2018**, *28*, 1804632.

53. Liu, X.; Yan, Z.; Zhang, Y.; Liu, Z.; Sun, Y.; Ren, J.; Qu, X., Two-Dimensional Metal–Organic Framework/Enzyme Hybrid Nanocatalyst as a Benign and Self-Activated Cascade Reagent for in Vivo Wound Healing. *ACS Nano* **2019**, *13*, 5222–5230.

54. Liu, S.; Wang, B.; Yu, Y.; Liu, Y.; Zhuang, Z.; Zhao, Z.; Feng, G.; Qin, A.; Tang, B. Z., Cationization-Enhanced Type I and Type II ROS Generation for Photodynamic Treatment of Drug-Resistant Bacteria. *ACS Nano* **2022**, *16*, 9130–9141.

For Table of Contents Only

